THE ASTROPHYSICAL JOURNAL, 561:69–81, 2001 November 1

HYDRODYNAMIC DRAG IN COSMOLOGICAL SIMULATIONS

ERIC R. TITTLEY[1]
University of Maryland, Baltimore County, Joint Center for Astrophysics, Baltimore, MD, 21250; etittley@jca.umbc.edu
F. R. PEARCE
The School of Physics and Astronomy, University of Nottingham, Nottingham, NG7 SRD, DH1 3LE, UK; Frazer.Pearce@nottingham.ac.uk
AND
H. M. P. COUCHMAN[1]
McMaster University, Department of Physics and Astronomy, Hamilton, ON, L8S 4M1, Canada; couchman@physics.mcmaster.ca
Received 2001 May 8; accepted 2001 July 9

ABSTRACT

We present a study of hydrodynamic drag forces in smoothed particle hydrodynamic (SPH) simulations. In particular, the deceleration of a resolution-limited cold clump of gas moving through a hot medium is examined. The drag at subsonic velocities exceeds that expected from simple dynamics-based arguments. The excess is shown to be a result of the hydrodynamic method. SPH encourages the accretion of particles from the hot medium on to a shell around the cold clump, effectively increasing the radius of the clump. For sonic and supersonic velocities, the effective area of the clump is shown to be set by the symmetrized smoothing length. The relationship of the effective area to the smoothing length breaks the expected dependency of drag on density since the symmetrized smoothing length increases with decreasing density. The consequences for cosmological simulations are discussed.

Subject headings: galaxies: clusters: general — galaxies: kinematics and dynamics — hydrodynamics — large-scale structure of universe — methods: numerical

1. INTRODUCTION

Numerical simulation has proved to be a powerful tool for understanding the dynamics and formation history of cosmic structure (Davis et al. 1992; Katz 1992; Cen et al. 1994; Evrard, Metzler, & Navarro 1996). When N-body techniques are combined with a hydrodynamical method to follow the baryonic component, further advancements can be made as now no additional assumptions are required to relate the baryonic material to the underlying collisionless matter. Such a combination has proved to be both a popular and powerful technique (Hernquist & Katz 1989; Evrard 1990; Katz & Gunn 1991; Cen 1992; Navarro & White 1993; Steinmetz & Müller 1993; Ryu et al. 1993; Bryan et al. 1994; Gnedin 1995; Steinmetz 1996). A common method of implementing hydrodynamics in N-body simulations is through the use of smoothed particle hydrodynamics (SPH) (Gingold & Monaghan 1977; Lucy 1977). The great strength of SPH is that it is a Lagrangian technique; individual particles act as tracers of the flow and better resolution can therefore be achieved in regions of high tracer density. This behavior is a very desirable property for cosmological simulations where extremely large density contrasts are present and excellent spatial resolution needs to be achieved within relatively large volumes.

In the standard model of cosmological structure formation, larger structures are formed via the amalgamation of smaller structures formed at earlier times. The structure building occurs in a hierarchical fashion. In any simulation in which structures form in this hierarchical manner, there will be an abundance of objects formed at the resolution limit of the simulation. The formation of these objects may be avoided by the removal of the high-frequency waves beyond a cut-off much lower than the Nyquist frequency, but this removes the structure that is of interest and alters fundamental scaling relations (Tittley & Couchman 1999). A particularly difficult problem is following these small, resolution-limited halos as they are subsumed into larger structures as the hierarchy progresses. It has been found that much of the substructure in collisionless simulations is erased unless very high resolution is employed (Ghigna et al. 1998; Moore et al. 1999; Klypin, Gottlüober, & Krastov 1999). The loss of substructure is the classic overmerging problem (White 1976; van Kampen 1995; Summers et al. 1995; Moore, Katz, & Lake 1996).

With the inclusion of radiative cooling into the hydrodynamic model, the baryonic material can dissipate energy and become more tightly bound than the dark matter, allowing individual objects to survive the hierarchical process that builds up large structures (Summers et al. 1995; Frenk et al. 1996). Klypin et al. (1999) argue that these objects are not likely representative of bound gaseous structures in nature, since they are lacking the dark-matter halos observed to dominate similar structures (Persic, Salucci, & Stel 1996). As well, the dynamics of this set of objects may now be affected by gas forces; as Frenk et al. (1996) demonstrate, the viscous drag due to the passage of a galaxy-sized object through the hot intracluster medium of a cluster can be sufficient to cause much of the material to spiral into the center of the cluster.

For example, consider the simple model of a clump of cold gas, embedded in a dark-matter halo, falling into the potential well of a cluster. The significance of the hydrodynamics and the resolution of the simulation is demonstrated in Figure 1. The figure illustrates the passage through a 10^{15} $M_{\odot}$ mixed-matter halo of a galaxy-group-sized halo comprised of, alternately, (1) only dark matter (1.5×10^{12} $M_{\odot}$); (2) only gas (2.3×10^{11} $M_{\odot}$); and (3) both dark matter and gas. The systems were simulated at resolutions spanning

[1] Much of this work was done at University of Western Ontario, Department of Physics and Astronomy, London, ON, N6A 3K7, Canada.

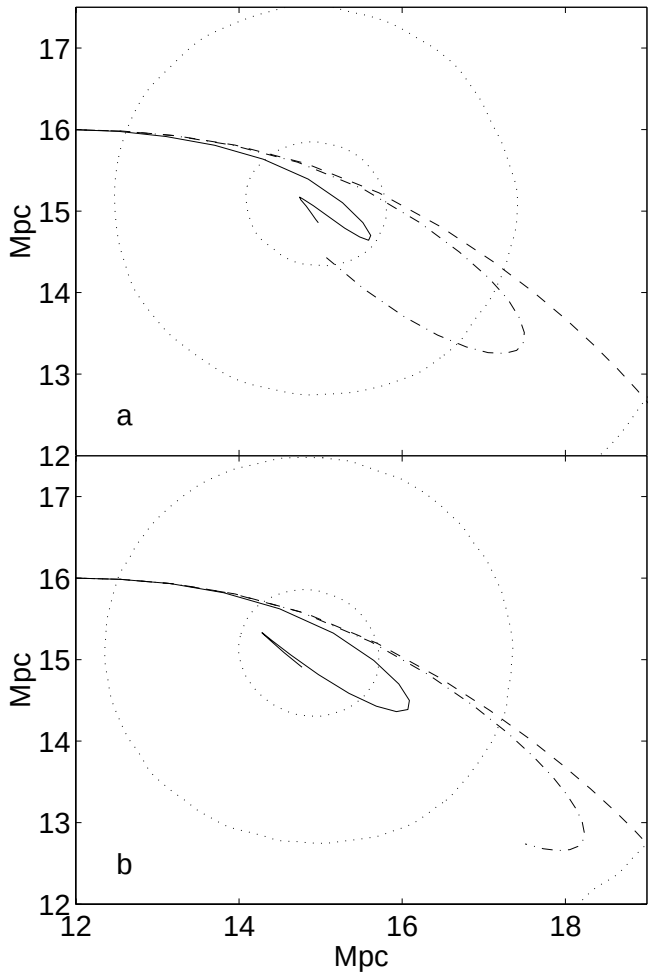

FIG. 1.—Path of clumps through a cluster halo. The data are given for two resolutions corresponding to $m_g = 7.7$ and $1.2 \times 10^9\ M_\odot$ (panels [*a*] and [*b*], respectively). In each panel, three paths are plotted corresponding to a purely collisionless halo (*dashed line*), a purely gaseous halo (*solid line*), and a mixed-matter halo (*dot-dashed line*). The isodensity contour lines are for gas densities of 10^{-29} and 10^{-28} g cm $^{-3}$. The dark-matter particles are 6.5 times more massive and equally as abundant as gas particles. The clump starts at the left, traveling to the right at 1000 km s $^{-1}$ ($\approx$1 Mpc Gyr,$^{-1}$) with an impact parameter of 1 Mpc, and is followed for 1 Gyr.

almost a decade in mass resolution. The number of particles in the cluster halo were either 30 or 200 thousand. The numeric softening was kept constant for both resolutions, effectively fixing the cross section of the clump. The constancy of the cross section proves an important point: the decrease in drag is not due simply to the clump being smaller at higher resolutions. The details of the simulation method are saved for later. What is important to note is that for the most realistic scenario (that of the combined dark-matter–gas halo), the forces on the clump are dominated by those on the dark-matter halo. That is to say, the gas is bound to the dark matter and goes where the dark matter takes it. For the gas halo on its own, the drag forces are much more significant and pull the clump rapidly into the center of the cluster halo. The drag rate is also clearly affected by the resolution of the halo, increasing the drag at lower resolutions. The increase in drag also affects the trajectory of the mixed-matter clump, revealing that the resolution does vary the deceleration rate of the more realistic structures. Furthermore, the discrepancy between the path of the gas-only clump and the mixed-matter clump cannot be attributed to the mass difference only, since a collisionless clump of the same mass as the gas-only traces nearly the same path as the more massive collisionless clump illustrated in Figure 1.

There is a discrepancy in the importance of drag between the simulations of Frenk et al. (1996) and those of Katz et al. (Katz, Hernquist, & Weinberg 1992; Katz, Weinberg, & Hernquist 1996). Those of Frenk et al. find the viscous drag causes galaxy-sized objects to spiral into the center of the cluster. The simulations of Katz et al. have little difference in the merger rate of galaxy-sized substructure in simulations of cluster formation in which the galaxies are modeled by either collisional or collisionless matter. The difference may be due to the survival rate of the dark-matter halos in which the galaxies are embedded. If these halos evaporate owing to numerical effects (two-body interactions, particle-subhalo heating, etc.), then the baryonic material will quickly be consumed into the center of the cluster. Neither set of authors describes the survival of their dark-matter halos, so the discrepancy is not yet resolved. What is clear is that other effects, both physical and numerical in nature, not related to the SPH algorithm have an impact on the survival and merging of substructure in halos. A study of these pure N-body effects is beyond the scope of this paper and, indeed, has been done in a thorough manner elsewhere (Carlberg 1994; van Kampen 1995; Moore et al. 1996; Ghigna et al. 2000). This paper will concentrate on the contribution of hydrodynamic drag for resolution-limited objects, with particular attention to numerical effects.

Previous work has shown that numerical effects, at work in SPH simulations, lead to excessive drag. In Thacker et al. (2000), tests of a variety of implementations of SPH are described. The implementations varied in the method of force symmetrization, the form of the artificial viscosity, and the presence of a shear-correction term in the artificial viscosity. They were compared by probing the behavior of the SPH implementations in a series of scenarios relevant to cosmological simulations. Included in this series is the drag experienced by a cold clump traveling through a hot medium. It was concluded that the drag on the cold clumps is excessive when SPH is used, independent of the implementation method. The reason for this behavior was not explored, nor was the behavior extensively characterized.

Ritchie & Thomas (2001) describe multiphase-SPH (SPHM), a modified SPH that alleviates the problems encountered when gases widely separated in the ρ-T plane intermix. The modifications were introduced primarily to contend with the supercooling phenomenon brought on in SPH simulations when a hot gas surrounds a dense, cool clump of gas. The hot gas, when encountering the cold clump, has its SPH density estimate abruptly rise, significantly lowering the cooling time. As will be shown, the numerical process that leads to this supercooling is intimately related to the process that increases drag in subsonic clumps. Consequently, the drag experienced on the clumps using SPHM should be decreased. The expectation is indeed the case, as Ritchie & Thomas show. They leave it to us to describe the numerical processes that lead to the overproduction of drag in the first place.

This paper is an extension of the drag tests described in Thacker et al. (2000). In this paper we investigate the numerical processes that control the strength of the viscous

drag of a hot medium on a resolution-limited cold clump of gas within a smoothed particle hydrodynamic (SPH) method. This study is accomplished through the use of numerical simulations of the simple scenario in which a cold gaseous halo is passed through a hot, uniform medium. Three velocity regimes are explored: subsonic, sonic, and supersonic. Analysis is assisted by a comparison of the actual deceleration observed for our clumps with that predicted from simple theoretical arguments.

The models for the clumps are intentionally simple. We study what are essentially resolution dominated spheres of material moving within a uniform density hot medium. Such objects are typical of the galaxies or groups of galaxies formed in cosmological simulations of structure formation where most of the objects have masses and physical extents near to the resolution limit of the simulation (Pearce et al. 1999). It is important to note that regardless of the resolution, without removal by modification of the initial power spectrum, resolution-limited structures will form and play a role in the development of the larger structures.

The paper is laid out as follows. The details of the numerical method are given in § 2. The expected drag is given in § 3 as well as the description of how the drag derived from the models is compared to the expected. The model clump-halo systems are described in § 4. A comparison between the expected and the actual deceleration found in our models for a variety of Mach numbers is presented in § 5 and discussed in § 6. In the Appendix we give the details of the expected drag.

2. NUMERICAL METHOD

The implementation of SPH used here is based on the N-body hydrodynamic code, *hydra* as described in Thacker et al. (2000). A complete description of the methods for generating the symmetrical hydrodynamic forces is also contained in Thacker et al..

For some of the tests (described in § 4), the method for symmetrization of the hydrodynamic forces in the SPH code was varied. The options explored are symmetrization via averaging the smoothing kernels, $W(r_{ij}, h_i)$ and $W(r_{ji}, h_j)$, calculated for each pair of particles or averaging the smoothing lengths, h_i and h_j, of each pair and then using only the one kernel value, $W(r_{ij}, h_{ij})$. For the rest of the tests, symmetrization of the force equation is provided by arithmetic averaging of the smoothing lengths.

The smoothing lengths, h_i, are updated on a per-iteration basis. The update is accomplished by weighting the previous value by a factor that is a function of the actual number of neighbor particles, $N_{\rm neigh}$, found during the iteration, within the radius of $2h$. Consequently, $N_{\rm neigh}$ generally approximates $N_{\rm SPH}$ but does not often equal $N_{\rm SPH}$ unless it is in a region of the simulation volume where the dynamic timescale is far greater than the iterative timescale. For regions where the dynamic timescale is short, a limit is placed on the iterative timescale. The goal of the iterative approach is to prevent $N_{\rm neigh} \ll N_{\rm SPH}$, which is achieved remarkably well ($N_{\rm neigh}$ is never less than $0.8N_{\rm SPH}$ in a rotating cloud test (Thacker et al.). In practice, there is also a minimum value of h_i at the resolution limit, so $N_{\rm neigh} \gg N_{\rm SPH}$ in regions of high density.

We use a Monaghan-type artificial viscosity. Since it was demonstrated in Thacker et al. that the general behavior of the drag is not affected by the presence of a Balsara term (Balsara 1995), which reduces the viscosity in the presence of shear, one was not included in the implementation of SPH used.

The gas was not cooled radiatively. Cooling could lead to accretion of particles on to the cold clumps, which would make the analysis more difficult.

For the calculation of the gravitational forces, *hydra* uses an adaptive particle-particle, particle-mesh method ($\rm AP^3M$; Couchman 1991). The minimum resolution is set by the gravitational softening length, which is 72 kpc. The minimum value for the smoothing length parameter, h_i, is $\frac{1}{2}$ of the gravitational softening length.

All forces are periodic across the boundaries of the simulation cube.

3. EXPECTED DECELERATION

There are two important caveats to any calculation of the expected drag. Since this paper examines the forces on resolution-limited objects, an estimate of the expected deceleration must necessarily ignore many physical phenomena that could also disrupt the objects and alter their deceleration. For example, ram-pressure stripping and ablation due to the Kelvin-Helmholtz instability would remove material from the infalling clumps. These processes can occur on a timescale shorter than the dynamic scale of substructure in clusters. Dwarf galaxies, for example, lose material as a result of ablation in about 2 Gyr (Ga) (Mori & Burkert 2000), with only a weak dependence on the total initial mass of the galaxy. The mass-loss rate by this process is related to the force of drag and the clump velocity simply by $\dot{M} \approx F_D/V$ (Nulsen 1982). The relation implies the timescale of deceleration, $t_D = MV/F_D$, is equal to the mass-loss timescale, $t_{\dot{M}} = M/\dot{M}$. In the opposite sense, cooling of the gas on to the clump (Balsara, Livio, & O'Dea 1994) and ultimately into stars retards mass loss, though feedback from the subsequent supernovae heats the gas, gravitationally unbinding it. However, these processes could only be modeled in simulations if the objects were *resolved*, which is not our present concern, here. Consequently, *we will focus simply on the drag felt by a solid sphere that is at the resolution limit of the SPH simulation.*

The second caveat pertains to the estimate of drag, itself. The force felt on the object is a combination of deceleration due to specular reflection, diffuse reflection, accretion, and evaporation. Even presuming that the last two are nil, there are no comprehensive data available in the literature concerning the relative fraction of specular and diffuse reflection for combinations of materials and media encountered in laboratories (Chen 1997), let alone in astrophysics. *The estimate of the drag presented here should only be taken as an approximation in amplitude and in form.*

It is not necessary to deduce the true drag that would be felt by such an object in order to characterize the numerical effects since, over the relatively narrow range in velocities explored (about a decade), the estimated and measured drag should differ only by a constant factor. That is to say, if the numerics are not introducing any velocity-dependent effects, the drag should be correct to within a normalization constant with the error coming from either non-velocity dependent numerical effects or errors in the determination of the proper drag equation.

The only important parameters relating to the sphere are its radius, R, and the velocity, V, relative to the medium. The significant parameters of the gas are its density, ρ_g, and temperature, T. The drag is a function of R, V, and ρ_g, as

well as the coefficient of drag for a sphere, C_D. The coefficient of drag, in turn, is a function of the Reynolds number, Re, which is a function of the size and velocity of the sphere, as well as the dynamic viscosity, η. The dynamic viscosity is peculiar only to the parameters of the enveloping medium and is the biggest unknown.

The drag on a sphere moving through a fluid medium at any speed is given by the expression

$$F_D = \tfrac{1}{2} C_D(\mathrm{Re}) \rho_g V^2 \pi R^2 , \quad (1)$$

where C_D(Re) is the coefficient of drag and is, itself, a function of velocity, particularly at low velocity (see eq. [A2]). The $\rho_g V^2 \pi R^2$ part of the expression is derivable simply by considering a bucket sweeping up all the material it encounters with the subsequent deceleration due to momentum conservation. In this simple case, $C_D = 2$.

Deviation from the simple bucket model can lead to larger or smaller drags. Since not all the gas that is swept up continues with the same forward momentum as the clump, the actual momentum required to accelerate the gas can be much less, leading to a lesser deceleration. On the contrary, the bow wave can extend the range of influence of the clump to larger radii than R, increasing the deceleration. Consequently, C_D, varies from greater than 10 to $\frac{1}{2}$ as the Reynolds number increases and must be calculated for each model system and clump velocity.

The full description and derivation of the equations for Re, C_D, and η used in the analysis are given in the Appendix.

Fitting equation (1), given F_D, V, and a calculated value for C_D appropriate to the velocity of the clump, gives an effective radius, R_{eff}. The value should be constant for a given model system, independent of velocity. It incorporates any normalization factor by which equation (1) may be off. Hence, *variation* in R_{eff} as other parameters are altered is in itself indicative of effects beyond those strictly hydrodynamic in nature.

A preliminary estimate of R_{eff} may be made as follows. For the clump particles, the smoothing length, h_{clump}, is set to the minimum allowable value, as determined by the gravitational softening length. We could just choose $R_{\mathrm{eff}} = 2h_{\mathrm{clump}}$. However, because of the symmetrization inherent in the SPH method, the smoothing length of the hot particles is also important and it is some combination of this length with the smoothing length of the cold particles that is required. We will assume that the appropriate radius is that radius at which the clump particles contribute an equivalent amount to the SPH density calculation for a hot gas particle as the hot particle itself. That is,

$$N_{\mathrm{clump}} W(R_{\mathrm{eff}}, h_{ij}) = W(0, h_{\mathrm{hot}}) \quad (2)$$

where we have assumed that all the cold clump particles are at essentially the same distance. Since $N_{\mathrm{clump}} \gg W(0, h_{\mathrm{hot}})$, this implies $W(R_{\mathrm{eff}}, h_{ij}) \simeq 0$, which gives $R_{\mathrm{eff}} \simeq 2h_{ij}$ since the kernel function, $W(r, h)$, is negligible only at $r \simeq 2h$. Hence, it is expected that the effective radius should be approximately twice the symmetrized smoothing length.

4. MODEL SYSTEMS

The tests in this paper are variations on the same theme: a cold clump moving through a hot medium. The clump may be allowed to slow or be forced to maintain a constant velocity, depending on the needs of the particular test. The sole exception to this theme is the clump-halo simulation, which is described below in set 4.

Our models attempt to mimic the conditions encountered as a resolution-limited cold clump of the size of a group of galaxies passes through the halo of a galaxy cluster. As noted in the introduction, the presence of a dark-matter halo impedes the deceleration of a clump in simulations due to the inertia it adds to the system. However, no dark-matter halo is included in these test simulations since (1) the cold gas is sufficiently bound by self-gravity to withstand stripping forces (see § 3 for the caveat concerning mass-loss) ; (2) the presence of a dark-matter halo would add complication to the analysis owing to the consequent dynamic friction it would experience.

The clumps of cold gas are essentially structureless spheres, lying at the resolution limit of the code. They represent the first (and most common) structures to form in a cosmological simulation of hierarchical clustering and are, consequently, the dominant source of material during the creation of larger structures (Fardal et al. 2000; Kay et al. 2000). The gas in the clumps is cold (10^4 K) since the dense gas cools rapidly to this temperature through a radiative process.

The clump sizes are large for their mass ($R \sim 70$ kpc), which is typical of unresolved structures in simulations of large-scale structure. As will be shown, the effective size of objects is determined significantly by the local number density of particles in the surrounding medium.

Within a typical cosmological simulation the halos of galaxy clusters are hot ($\lesssim 10^8$ K) and more diffuse than the cold clumps because the hot halo gas is sitting close to virial equilibrium within the cluster potential well. The hot halo of galaxy clusters are observed through the X-ray emission (see Horner et al. (1999), for examples). Consequently, the hot media in our models are at temperatures of 10^7 or 10^8 K and are 1/100 as dense as the cold clumps. Given the density and temperature differences, the pressure is 10–100 times greater in the hot medium than the cold clump. This is not a concern since at the resolution limit, one should not expect the pressure gradient to be resolved. Indeed, at distances much less than the radius of the smoothing kernel, typical of the separation of particles within the cold clump, the SPH pressure gradient is negligible regardless of the difference in temperature of particles.

The sound speed is approximated by

$$V_s = \left(\frac{\gamma \mathrm{k}\ T}{\mu m_u} \right)^{1/2} , \quad (3)$$

for which $\gamma = \frac{5}{3}$ for an ideal monotonic gas. The relation gives speeds of 484 and 1529 km s^{-1} for the 10^7 or 10^8 K gases, respectively. These velocities will be referenced nominally as 500 and 1500 km s^{-1}.

The hot gas is in a glass configuration. The gas was prepared from an initially random placement of particles which was subsequently allowed to relax to a stable state. The cold clump was created by randomly placing stationary gas particles within a sphere of radius equal to the gravitational softening length then allowing them to relax in isolation in response to both gravitational and hydrodynamic forces. The two systems were then combined.

The Jeans length, R_{J}, for the hot gas phases is sufficiently large to ensure stability even in the presence of the perturbation from the cold clump. The condition insures that dynamic friction should not be important. This expectation was confirmed by passing a collisionless clump through the

hot medium—it experienced negligible deceleration. For a discussion of dynamic friction in systems with hydrodynamics, see Ostriker (1999).

The models have periodic boundary conditions to maintain a uniformity of temperature and density in the hot medium. A box length of 2 Mpc was chosen so the cold clump was both well separated from its images (arising from the periodic boundary conditions) and would move across the box only once without encountering its own wake.

In total, 41 model systems in a total of six sets were examined:

Set 1: Drag versus Mach number.—The 12 models in this set each consist of a knot of 100 cold particles ($T = 10^4$ K) of total mass, $2 \times 10^{11}\ M_\odot$ moving through a uniform distribution of 13,000 hotter particles ($T = 10^7$ or 10^8 K). The radius of the clumps is determined by the minimum SPH smoothing length which is 36 kpc in these simulations. The velocities of the clumps were fixed and spanned 100 to 1000 km s^{-1} ($\mathscr{M} = 0.2$ to 2) in the 10^7 K gas and 150 to 2250 km s^{-1} ($\mathscr{M} = 0.1$ to 1.5) in the 10^8 K gas. The velocity of sound, V_s, in the media is either 500 or 1500 km s^{-1}, with the larger V_s corresponding to the hotter gas. The Jeans length for the hot media are 6 and 18 Mpc, respectively. The density contrast between the clump and the medium is 100 with a gas density of 2×10^{-28} g cm^{-3} for the hot medium. There is no dark matter.

Set 2: Effective radius versus particle number density.—The nine models used here are similar to those used in set 1. However, only three clump–hot-medium combinations were examined: $\mathscr{M} = \frac{1}{3}$ (500 km s^{-1} clump in a 10^8 K medium), $\mathscr{M} = 1$ (500 km s^{-1} clump in a 10^7 K medium), and $\mathscr{M} = 2$ (1000 km s^{-1} clump in a 10^7 K medium). Each combination was simulated three times, varying the number density of particles in both the clump and hot medium with the higher number densities being 2 and 5 times the initial number density. The mass density was not varied. The clumps were permitted to decelerate.

Set 3: Effective radius versus mass density.—Similar to set 2, for these nine models, the mass density was varied in the hot medium along with the number density. Consequently, the mass per particle was kept constant. Nothing was changed for the clump; it contained 100 particles only with the same mass per particle in each.

Set 4: Clump-halo simulation.—The set is the only one not based on a clump moving through a uniform, hot gas. For this set of seven simulations, already seen in the Introduction, a clump was injected into a cluster halo at 1000 km s^{-1} and allowed to decelerate. The clumps were composed of either gas and dark matter, just the dark matter, or just the gas. For each of these three clumps, simulations were performed twice with the mass resolution varied by a factor of ≈ 7 between the two. In the low-resolution simulations, the clumps had 30 particles of each species (for 60 total particles for the mixed cluster) and the halo had 15,000 of each. The mass per gas particle was $m_g = 7.7 \times 10^9\ M_\odot$ with the dark-matter particles being 6.5 times greater. For the higher resolution, there were 200 of each species in the clumps and 100,000 in the halo ($m_g = 1.2 \times 10^9\ M_\odot$). The clump gas was at a temperature of 10^4 K. The initial impact parameter of the clump was 1 Mpc at 3 Mpc distance from the cluster center. The cluster was simulated in a volume 30 Mpc on a side with isolated boundary conditions. A final, seventh, simulation was performed for which the clump was collisionless and of the same mass as the gas clump. This final simulation was performed for only the low-resolution case.

Set 5: Method of SPH symmetrization.—Similar to set 1, three systems were modeled, varying the method of symmetrization between them. The clumps had their velocities held at a constant velocity corresponding to the speed of sound in the hot medium. The methods of symmetrization implemented were kernel, arithmetic, and harmonic averaging schemes.

Set 6: Significance of clump size.—Also similar to set 1, two systems were modeled. In one, the gravity term was modified to contain a repulsive term that dominates at short distances. The term spreads the particles in the cold clump out within their smoothing radius. The long-range forces are unaffected. The second system used the regular gravitational force term.

5. RESULTS

Using the model clump-hot-gas systems described in § 4, a series of tests were performed to characterize the behavior of the drag in three velocity regimes: subsonic, sonic, and supersonic. The results of these tests are separated below into those that pertain to all velocity regimes and those that are peculiar to the subsonic.

5.1. *Viscous Drag at All Velocities*

Using the model systems on a set by set basis, the behavior of the drag is examined in detail with the emphasis on demonstrating the effect of various numerical effects.

5.1.1. *The Measured D versus the Fiducial Drag*

The equation for the fiducial drag, given by the analytic expression equation (1), can be used to determine those velocity regimes in which the drag is excessive, i.e., greater than expected. Measurement of the drag on the clump, when compared with the fiducial amount, delineates those velocities for which the drag is excessive. The measurements were accomplished using the series of tests in set 1 (described in § 4). The tests involved plowing a clump through a uniform medium at various fixed velocities.

The drag expected for the clump was compared to the measured drag by calculating the effective radius of the clump using equation (1) in the various velocity regimes. Note that the appropriate value for the coefficient of drag, C_D, is calculated for each velocity so the transition from $F_D \propto V^2$ to $F_D \propto V$ at low Reynolds number is implicitly modeled. The behavior of the drag is illustrated by Figure 2, which plots the effective radius, $R_{\rm eff}$, versus Mach number. The effective radius, and consequently the effective cross section of the clump, is much larger than the estimated value of $2h_{ij}$ at speeds less than $\mathscr{M} = 1$. Significantly, the deviation is dependent on the Mach number only, not the velocity or the temperature of the hot media. The lack of dependency on velocity demonstrates the velocity scale invariance of the results presented in this paper.

At supersonic speeds there is an apparent convergence of the effective radius to the expected radius, $2h_{ij}$. For the entire range, $0.2 < \mathscr{M} < 2$, but particularly for $\mathscr{M} < 1$, the effective radius follows the simple relation

$$\frac{R_{\rm eff}}{h_{ij}} = (2.4 \pm 0.2)\mathscr{M}^{-1/2}\ , \qquad (4)$$

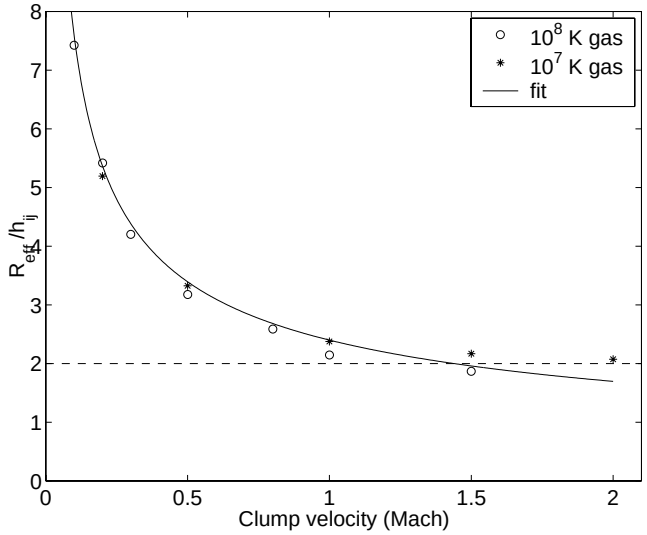

FIG. 2.—Effective radius of the clump as it varies with Mach number. The data are given for both the 10^8 K ($V_s = 1500$ km s^{-1}; *open circles*) and 10^7 K gas ($V_s = 500$ km s^{-1}; *asterisk*). The fit made to the curve is discussed in the text. The line at $R_{\rm eff} = 2h_{ij}$ is the expected value.

which is also illustrated in Figure 2. However, while this goes to zero at large Mach numbers, the data are consistent with $R_{\rm eff}$ bottoming out at $2h_{ij}$ for $\mathscr{M} > 1$.

The excessive drag at subsonic speeds manifests itself in Figure 2 as a rapidly increasing effective radius toward lower speeds. We will return to this point in § 5.2, where the cause of this phenomenon will be explored.

5.1.2. *The Scaling of the Drag with the Averaged Smoothing Length*

If the effective radius of the clump is truly set by the radius of the combined smoothing length, h_{ij}, as is argued in § 3, then the drag on the clump should scale with this length. To test this, the clump was passed through three media of the same physical density, but differing number density, $n_{\rm hot}$, of hot gas particles (set 2 of simulations as described in § 4). Since the smoothing length, $h_{\rm hot}$, scales with $n_{\rm hot}^{1/3}$, this varies the mean smoothing length of the hot gas and consequently the combined smoothing length, h_{ij}. The test was done for number density increments of two and five times. In these tests, which were performed for the velocity regimes of Mach $\frac{1}{3}$, 1, and 2, the clumps were permitted to decelerate instead of being held at constant velocity as was done for the tests in the previous section.

For each of the tests, an effective radius, $R_{\rm eff}$, was determined by integrating the equation of motion, $\dot{V} = -F_D(V, R_{\rm eff})$ with F_D given by equation (1), and solving for the best fitting value of $R_{\rm eff}$. The results, given in Table 1, support the hypothesis that the effective radius does indeed scale with the averaged smoothing length, h_{ij}. In each velocity regime, the effective radius is approximately a constant multiple of the averaged smoothing length (fifth column), particularly for the supersonic case. The correlation is not strong enough to be distinguished from scaling with just the smoothing length of the hot gas, $h_{\rm hot}$ (fourth column), owing to the error in the fitting of $R_{\rm eff}$. It is clear, however, that the effective radius does not scale with the smoothing length of the clump particles (third column).

Though the effective radius is a similar factor of the averaged smoothing length within each regime, the factor is different between each regime; $R_{\rm eff} \simeq 3$ for the Mach $\frac{1}{3}$ tests and 2 for both the Mach 1 and Mach 2 regimes, respectively. The trend to larger $R_{\rm eff}$ with increasing Mach is the same as outlined in § 5.1.1 and, in particular, Figure 2. The result for the Mach $\frac{1}{3}$ clumps further emphasizes the excessive amount of drag found in the subsonic regime.

TABLE 1

SCALING OF R_{eff} AS NUMBER DENSITY VARIES

$n_{\rm hot}$	$R_{\rm eff}$ (Mpc)	$R_{\rm eff}/h_{\rm clump}$	$R_{\rm eff}/h_{\rm hot}$	$R_{\rm eff}/h_{ij}$
		Mach $\frac{1}{3}$		
×1.....	0.26 ± 0.01	7.1 ± 0.3	2.6 ± 0.1	3.8 ± 0.1
×2.....	0.20 ± 0.01	5.4 ± 0.3	2.5 ± 0.1	3.4 ± 0.2
×5.....	0.16 ± 0.01	4.3 ± 0.3	2.7 ± 0.2	3.3 ± 0.2
		Mach 1		
×1.....	0.19 ± 0.01	5.1 ± 0.2	1.9 ± 0.1	2.8 ± 0.1
×2.....	0.15 ± 0.01	4.0 ± 0.3	1.9 ± 0.1	2.5 ± 0.2
×5.....	0.08 ± 0.005	2.2 ± 0.1	1.4 ± 0.1	1.7 ± 0.1
		Mach 2		
×1.....	0.14 ± 0.01	3.8 ± 0.3	1.4 ± 0.1	2.0 ± 0.1
×2.....	0.13 ± 0.01	3.5 ± 0.3	1.6 ± 0.1	2.2 ± 0.2
×5.....	0.09 ± 0.005	2.4 ± 0.1	1.5 ± 0.1	1.8 ± 0.1

5.1.3. *The Scaling of the Effective Cross Section with Local Density*

The results of the drag tests involving the deceleration of a clump through media of varying number density (§ 5.1.2) indicate that the drag felt on a clump traveling in the outer halo of a gravitationally bound system will be increased owing to the low number density of particles in this part of the halo. As the clump travels into denser parts of the halo, the apparent cross section will be reduced owing solely to the increased number density of the surrounding particles. The reduction in cross section should offset to a degree the increase in drag that the clump would be expected to feel as a result of the increase in the physical density. The force of drag in equation (1) is related to the effective radius and the local gas density via $F_{\rm drag} \propto -R_{\rm eff}^2 \rho_{\rm hot}$. Since we have the relations, $R_{\rm eff} \propto h_{ij} \propto n_{hot}^{-1/3}$, then $R_{\rm eff} \propto \rho_{\rm hot}^{-1/3}$ may be derived. This last relation implies that the drag force for the clump scales with the local gas density as $F_{\rm drag} \propto \rho_{\rm hot}^{1/3}$.

The previous result concerning the unphysical scaling of drag with local gas density assumes $h_{ij} \propto h_{\rm hot}$, an approximation that is always true for force symmetrization by kernel averaging and true for symmetrization by arithmetic averaging only for $h_{\rm hot} \gg h_{\rm clump}$. For harmonic averaging of the smoothing lengths, this reduction in drag as density increases is only partially effective for small $h_{\rm hot}$ and disappears for $h_{\rm hot} \gg h_{\rm clump}$. Geometric averaging leads to a different relationship, $F_{\rm drag} \propto \rho_{\rm hot}^{2/3}$, which is closer to the form normally expected.

To verify that this phenomenon occurs, a set of tests similar to those in § 5.1.2 were performed but with the mass resolution held constant while the number density is varied (set 3 of the simulations described in § 4). Hence, the clump was plowed through material of both different physical densities as well as number density. Since the velocity of sound varies only with the temperature of the gas, varying the mass density does not change the Mach number.

The measured deceleration for the clump in each test was then fitted to the equation of motion in the same fashion as described in § 5.1.2. The analysis produced an effective radius, which was then normalized by the smoothing radii

of the clump and the hot particles as well as their averaged value. If the effective radius still scaled with the averaged smoothing radius, h_{ij}, then the offsetting phenomenon would be verified. The tests and analysis were done for hot media with physical densities of 1, 2, and 5 times that employed in § 5.1.2 for the velocities corresponding to Mach $\frac{1}{3}$, Mach 1, and Mach 2.

The results of the analysis, summarized in Table 2, confirm that as the density contrast between the clump and the background density decreases, the effective radius still scales most closely with h_{ij}. Again the scaling is best for the supersonic clump, indicating some other process is occurring in the subsonic case. We will explore this other process in § 5.2. As a consequence of the scaling with h_{ij}, the force of drag approximately scales with $\rho_{\rm hot}^{1/3}$ in SPH simulations which employ symmetrization by either kernel averaging or arithmetic averaging of the smoothing lengths.

5.1.4. *The Method of Force Symmetrization*

Since the effective radius of the clump scales with the averaged smoothing length, h_{ij}, it is to be expected that the method of force symmetrization, which requires the use of an averaged smoothing length, should affect the drag. We examine this dependence in this subsection.

For h_{ij} calculated by arithmetic, harmonic, or geometric averaging, arithmetic averaging will always produce the largest value of h_{ij} while harmonic averaging leads to the smallest. Averaging the kernels themselves does not lend itself to such a comparison, since the effective value of h_{ij} would be dependent on r. However, using the argument to estimate $R_{\rm eff} \simeq 2h_{ij}$ outlined in § 3, for kernel averaging we have $h_{ij} \simeq h_{\rm hot}$, which is a maximum. Figure 3 verifies that at large radii, averaging the kernels indeed leads to the larger weighting and, hence, the largest degree of interaction.

For models with $h_{\rm hot}/h_{\rm clump} = 2.7$, the differences between the method of force symmetrization should be quite appreciable; averaging the kernel produces an estimated radius of interaction almost twice that of harmonic averaging of the smoothing radii. The result is consistent with the results of Thacker et al. (2000) in trend, if not magnitude, in which it is noted that averaging the kernels leads to the largest drag at velocities less than Mach 1 while harmonic averaging of the smoothing lengths leads to the least.

TABLE 2

SCALING OF R_{eff} AS MASS DENSITY VARIES

$\rho_{\rm hot}$	$R_{\rm eff}$ (Mpc)	$R_{\rm eff}/h_{\rm clump}$	$R_{\rm eff}/h_{\rm hot}$	$R_{\rm eff}/h_{ij}$
		Mach $\frac{1}{3}$		
$\times 1$.....	0.34 ± 0.1	9.0 ± 0.2	3.3 ± 0.1	4.9 ± 0.2
$\times 2$.....	0.32 ± 0.1	8.4 ± 0.1	4.0 ± 0.1	5.4 ± 0.1
$\times 5$.....	0.30 ± 0.1	8.0 ± 0.1	5.1 ± 0.1	6.2 ± 0.1
		Mach 1		
$\times 1$.....	0.17 ± 0.1	4.5 ± 0.1	1.7 ± 0.1	2.5 ± 0.1
$\times 2$.....	0.16 ± 0.1	4.4 ± 0.1	2.1 ± 0.1	2.8 ± 0.1
$\times 5$.....	0.15 ± 0.1	4.0 ± 0.2	2.5 ± 0.2	3.1 ± 0.2
		Mach 2		
$\times 1$.....	0.14 ± 0.1	3.9 ± 0.1	1.4 ± 0.1	2.1 ± 0.1
$\times 2$.....	0.13 ± 0.1	3.5 ± 0.1	1.6 ± 0.1	2.2 ± 0.1
$\times 5$.....	0.12 ± 0.1	3.1 ± 0.1	2.0 ± 0.1	2.4 ± 0.1

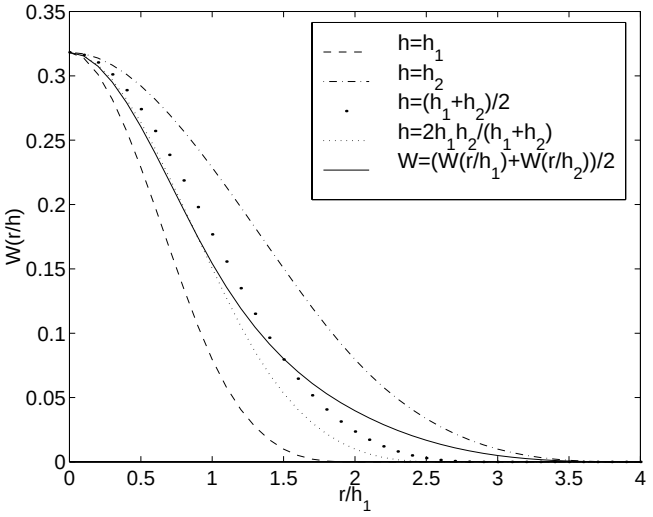

FIG. 3.—Kernel function for differing effective smoothing lengths. Plotted are the kernel functions for the symmetrizations of h via the arithmetic mean (*large dots*) and harmonic mean (*small dots*) when $h_2 = 2h_1$. The kernel functions using just h_1 and h_2 are also given (*dashed and dot-dashed lines, respectively*). The effective kernel function for the average of these two kernels is also plotted (*solid line*).

The drag on a constant-velocity Mach 1 clump was measured while varying the method of symmetrization. The simulation corresponds to set 5 as described in § 4. The implementations used kernel, arithmetic, and harmonic averaging schemes. Drags of 1.4×10^{36}, 1.0×10^{36}, and 0.6×10^{36} dyne were measured respectively. The test was not performed for geometric averaging of the smoothing lengths since this method produces a value for h_{ij} intermediate between arithmetic and harmonic averaging. The results confirm the trend that larger values for h_{ij} produce a greater drag, with the kernel-averaging scheme producing the largest mean drag, 2.4 times that produced with harmonic averaging and 1.4 times larger than that found with arithmetic averaging. However, since the drag should scale with $R_{\rm eff}^2$, kernel averaging should produce four times as much drag, instead of the 2.4 measured. The discrepancy indicates that there are secondary effects produced by the method of symmetrization that, for these tests, offset the direct connection between h_{ij} and drag. However, it is clear that the choice of method for force symmetrization significantly affects the amount of drag incurred.

5.1.5. *Energy Deposition*

The energy lost by the deceleration of the clump goes primarily into heating the surrounding gas. Since this gas is already hot, this extra thermal energy is absorbed without any significant change in the temperature of the gas. The total energy of the clump is less than 1% of the total thermal energy of the hot gas. The spatial distribution of this deposition of energy into the hot gas can be examined by looking at the *change* in temperature of the gas particles, illustrated in Figure 4. As expected, a bow shock is formed in the sonic and supersonic cases. On account of the large filling factor of the shock, it contains a large fraction of the deposited energy. Energy is also deposited in the wake of the clump.

For the subsonic clump, a transitory pulse is created at the start of the simulation, which quickly dissipates. Subsequently, most of the energy is deposited locally and carried along with the clump.

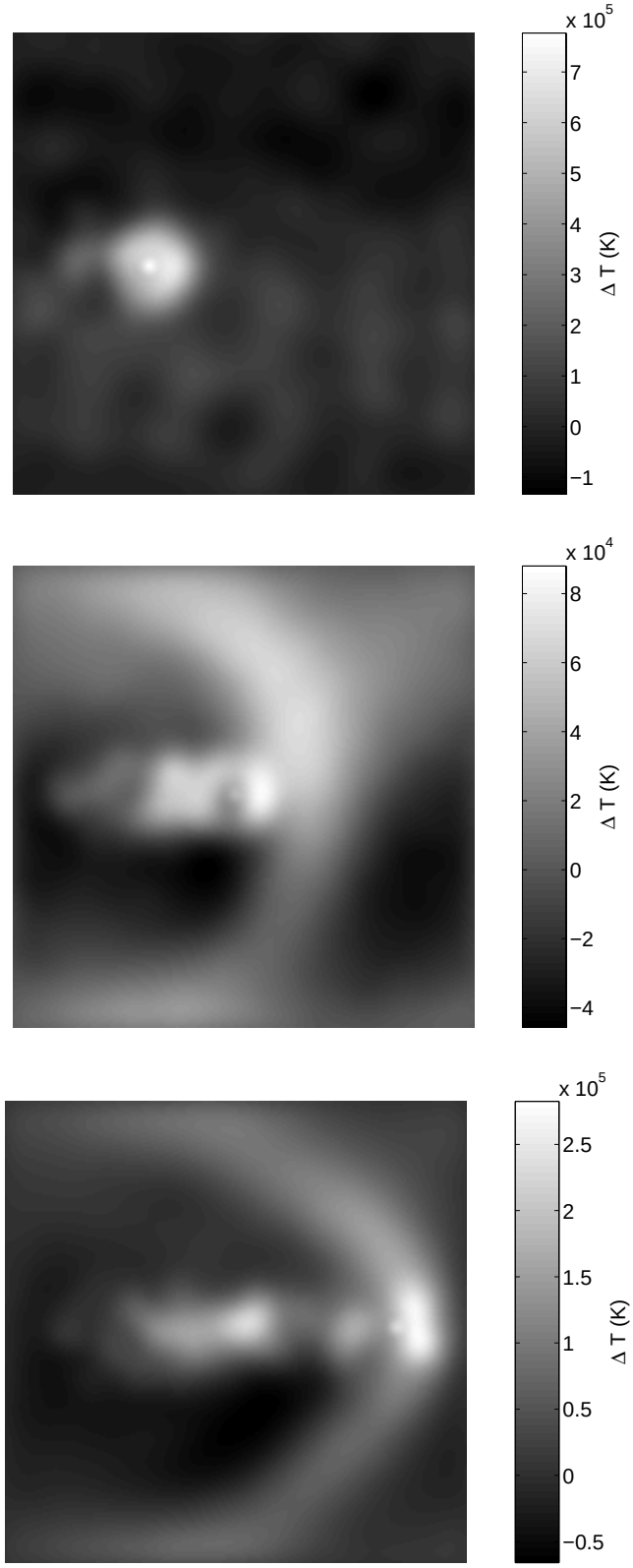

FIG. 4.—Temperature change in the hot gas due to the passage of the clump. The temperature changes for the gas is plotted for the Mach $\frac{1}{3}$ (*top*), Mach 1 (*middle*), and Mach 2 clumps (*bottom*). White indicates a larger temperature increase, black indicates no change. Note that the temperature changes are small compared to the actual temperature of the gas (10^5 K, cf. 10^7 K). The clump starts at a position one-tenth of the box size from the left. The slices are $10h_{\rm clump}$ thick.

5.2. *Drag in the Subsonic Regime*

It was established in § 5.1.1 that subsonic clumps have disproportionately large effective cross sections. The excess is demonstrated by Tables 1 and 2 and Figure 2. Whereas the sonic and supersonic clumps always decelerate less than the fiducial rate, the subsonic clumps experience a greater drag than expected. We show in this section that the clump accretes a layer of hot gas particles into a shell at the effective smoothing radius, $2h_{ij}$, and it is this shell that enhances the drag. Furthermore, it is demonstrated that this accretion into a shell is a by-product of the SPH pressure calculation in the vicinity of a compact collection of cold particles coupled with the artificial viscosity, which damps rapid accelerations. In this configuration, the calculated force on a hot gas particle due to gas pressure causes oscillations in the hot particle's velocity, which triggers the viscosity term of the hydrodynamic forces, bringing the hot particle to rest relative to the moving clump. In the subsonic regime we expect the clump to accrete some material as it moves through the hot medium, but it is the increase in cross section due to this shell of accreted particles that causes the clump to slow excessively.

5.2.1. *The Accretion of Remoras*

We characterize the behavior of the drag on a subsonic clump using the data from § 5.1.2 in which a cold clump was allowed to decelerate in a uniformly dense medium of hot gas. The subsonic clump initially follows approximately the same deceleration curve as given by equation (1). The transition to a more rapid deceleration occurs as particles are accreted from the hot gas phase. Accretion of these particles is evident in Figure 5, which displays the flow of particles about the cold clump in the reference frame of the cold clump at various Mach numbers. No hot particles are decoupled from the flow of hot particles in the Mach 1 and Mach 2 simulations, while 44 are decoupled in the Mach $\frac{1}{3}$ run.

The particles picked up from the hot medium will be referred to as "remoras." Since remoras are also found about the subsonic clumps, which are not permitted to decelerate (as in § 5.1.1), it is clear that the accretion does not occur only as the clump slows to almost stationary, but occurs while the clump still has a significant velocity.

The remoras form a narrow shell about the clump at a radius equal to the effective smoothing radius, $2h_{ij}$. Note that in this section we are using simple arithmetic averaging for the combined smoothing length; that is $h_{ij} = (h_{\rm hot} + h_{\rm clump})/2$. The shell is indicated by Figure 5 and is verified in Figure 6, which plots the two-point correlation function about the clump particles. The correlation function of the hot gas particles (Fig. 6, *dashed line*) shows that the particles have preferential spacings typical of a glass distribution, but not at the distance of $2h_{ij}$, at which distance hot particles are found to be overabundant by a factor of 100. The tight span of radii in which the remoras are permitted to come to rest is demonstrated by the narrowness of the peak in the correlation function at h_{ij}, witnessed in Figure 6. The jump in the correlation function is 2 orders of magnitude and is located just beyond $2h_{ij}$ (70 kpc) with a width of 10 kpc or about 10% of $2h_{ij}$.

In SPH, the pressure forces on an individual particle, F_i, are summed symmetrically over all neighboring particle

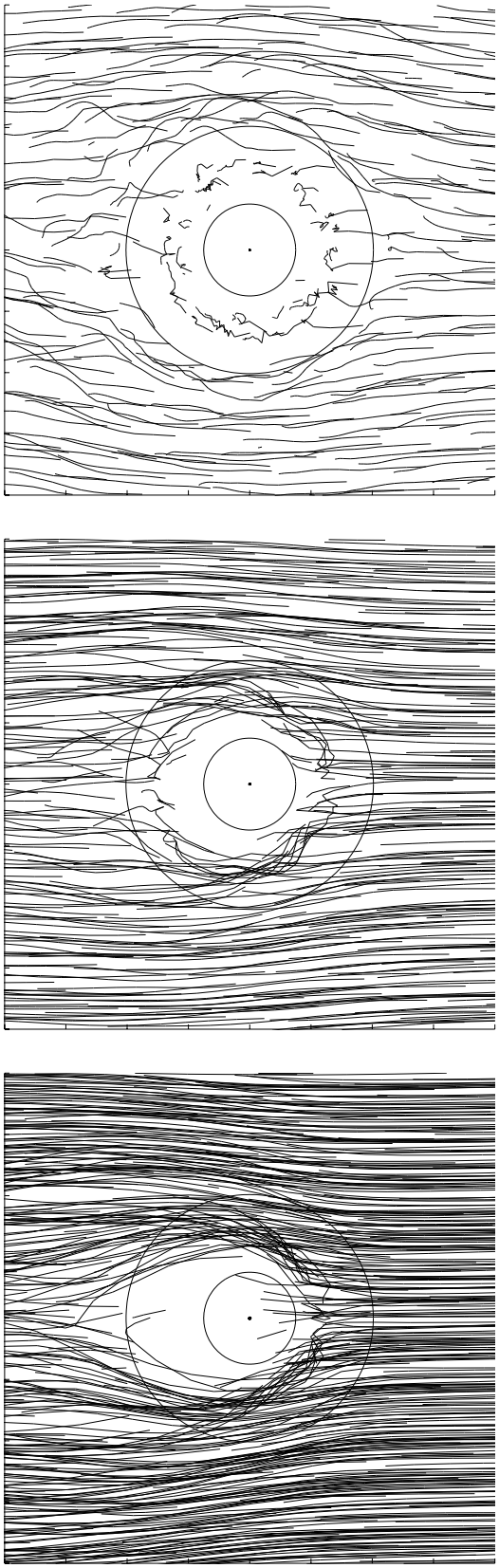

FIG. 5.—Flow of halo particles about clumps. The flows are plotted for the Mach $\frac{1}{3}$ (*top*), Mach 1 (*middle*), and Mach 2 clumps (*bottom*). The inner circle is the radius $2h_{\rm clump}$, while the outer circle is the same for the hot gas, $2h_{\rm hot}$. The effective smoothing length, h_{ij}, for this simulation is simply the arithmetic mean of h_i and h_j. Flow is from right to left. The slices are $5h_{\rm clump}$ thick.

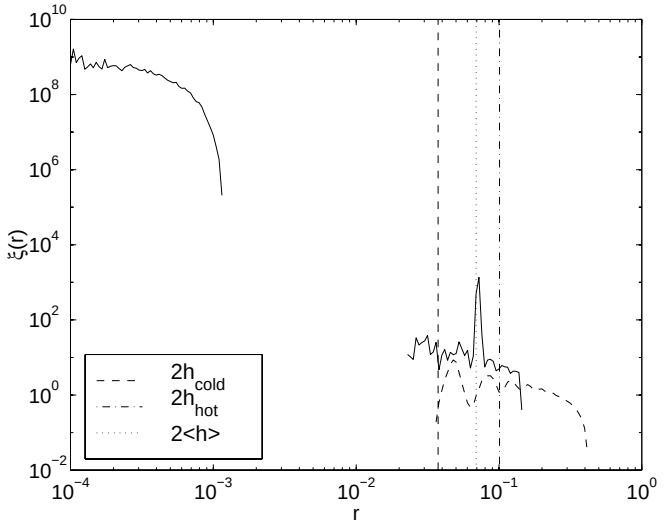

FIG. 6.—Two-point correlation function about the cold clump. Marked are the smoothing limits for the particles of the cold clump (*dashed line*), the hot gas (*dot-dashed line*), and the average (*dotted line*), which is the value used in these tests for a hot particle interacting with the cold clump. For comparison, the two-point correlation function for the hot gas away from the cold clump is given by the dashed curve.

pairs in the manner

$$F_i \sim \sum_j^N -m_i m_j \left(\frac{T_i}{\rho_i} + \frac{T_j}{\rho_j}\right) \nabla W(r_i - r_j,\, h_{ij}) \,. \quad (5)$$

The summation utilizes SPH's ability to estimate gradients of local scalar quantities by scaling the contributions from neighboring particles to the local values (the pressure, $P \sim \rho T$, here) by the gradient of the kernel function, W. The estimate is normally very effective when the local gradients in the temperature and, more significantly, the gas density, ρ, are small. While the temperature is a parameter incremented from the value from the previous iteration, ρ is a quantity re-estimated each time step. Hence, in the presence of the steep density gradients surrounding cold clumps, ρ can fluctuate significantly between iterations. If a hot gas particle is within twice its smoothing length, $2h_{\rm hot}$, of the centrally concentrated cold clump, then the estimated gas density will be significantly larger (1.5 times, for the implementation of SPH density estimates in *hydra*) for the particle than it would otherwise be.

It is informative to determine what the summation of the pressure forces is for a hot gas particle between $2h_{ij}$ and $2h_{\rm hot}$ from a cold clump. There will be two regimes: one in which the gas particle is at the far end of this distance, and the other when it is near $2h_{ij}$. In the first case, the hot gas particle will not be surrounded by a nearly isotropic distribution of particles. There will be a void on the side of the particle facing the cold clump. The two-point correlation function of the particles in the vicinity of the cold clump (Fig. 6) demonstrates the existence of this void, which occurs because particles are repelled by pressure forces close to the cold clump. The particles in the cold clump are centrally condensed within a radius much smaller than their SPH smoothing radius which is, in turn, half the gravitational softening radius (the minimum value we allow it to take). The void surrounds the clump and has a radius slightly smaller than the averaged smoothing radius. Hence, the gradient will force the particle toward the cold clump.

Once the particle is within $2h_{ij}$ of the cold clump it sud-

denly sees many more than $N_{\rm SPH}$ neighbors, so its smoothing length drops while its density estimate jumps. For a very diffuse hot medium, essentially all the neighbors of the particle are now in the cold clump, and the particle is repelled strongly by pressure forces. The kick the particle receives from the interaction with the cold clump is short-lived, and soon the unbalanced pressure force from the surrounding hot gas forces the particle back toward the clump starting the cycle again.

The cyclic, kick-drift phenomenon will occur even if the gas particles are able to see only a fixed number of neighbor particles, $N_{\rm SPH}$, since the motion of the hot gas particles relative to the clump will carry it rapidly between the domains dominated by the apparent void and that dominated by the cold clump. Even a substantial reduction in the iteration time step, to make the transition smooth, does not eliminate the contrast between the two domains.

A hot gas particle near a cold clump thus oscillates (or perhaps, more correctly, bounces) just beyond the radius, $2h_{ij}$. The oscillation is a consequence of the form of the SPH force calculations coupled with its treatment of neighbors and, as such, will be a characteristic of any standard implementation of SPH.

The path of a particle that is just grazed by the cold clump as it passes is shown in Figure 7. The path, in the reference frame of the cold clump, shows the series of accelerations described. What is even clearer is how these accelerations conspire to trap the particle at a radius approximately halfway between the smoothing radii for the clump and the hot gas.

In Figure 8, which plots the hydrodynamic forces for the hot gas particle in a direction perpendicular to the direction of motion of the clump, the alternating directions of the forces are clearly illustrated. In this figure, the density of the hot particle, as estimated by the SPH density calculation, is shown at the bottom. It clearly delineates the two regimes

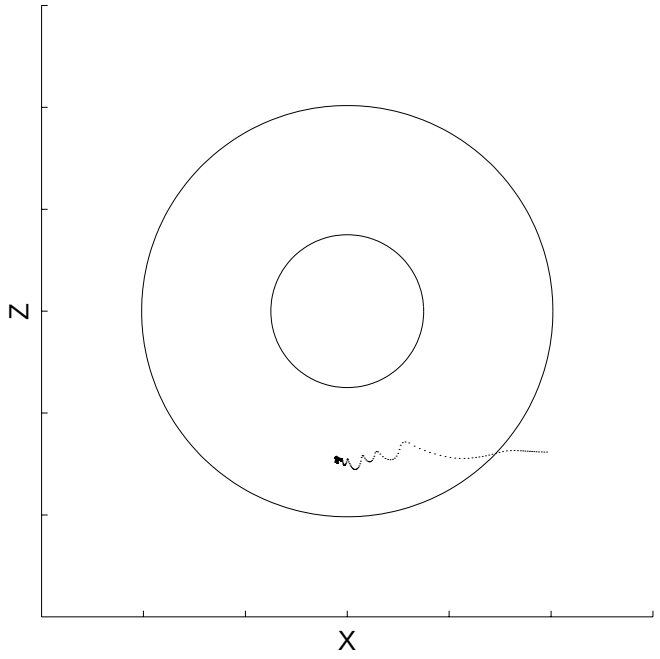

FIG. 7.—Path of a hot particle on to a cold, Mach $\frac{1}{3}$ clump. The position of the particle at successive iterations is plotted relative to the cold clump. Flow is from the right (the clump is moving right). The outer circle has a radius of $2h_{\rm hot}$, while the inner radius is $2h_{\rm clump}$.

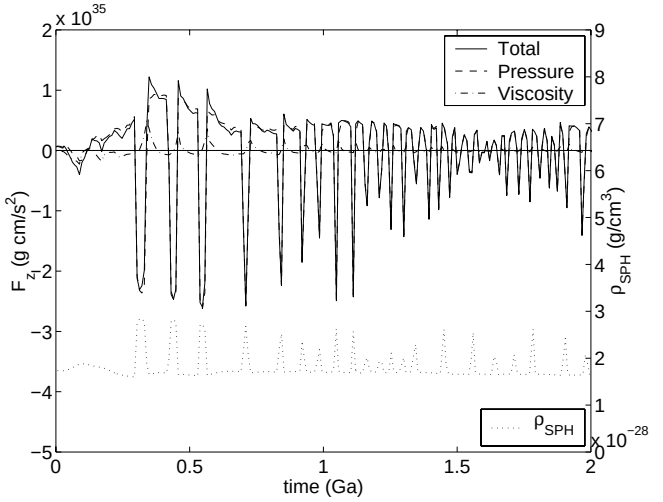

FIG. 8.—Forces on a remora particle in the direction perpendicular to the direction of travel. Plotted is the total force (*solid line*) as well as the contributions from the gas pressure (*dashed line*) and the artificial viscosity (*dash-dotted line*). The gas pressure provides the bulk of the instantaneous forcing and hence frequently overlaps the total force. Positive forces are directed toward the clump center. The gas density calculated by the SPH routine is shown by the dotted line, plotted against the right-hand axis.

described previously; when the density is low, the particle does not "see" the clump whereas when it is high, it is under the influence of the clump and feels a strong force away from it.

The oscillations between these two regimes are important as they trigger the artificial viscosity, which drags the particle into moving with the clump. As the viscosity is only triggered if two particles are converging, the particle is interacting viscously alternately with the clump and the hot gas. The viscosity damps the oscillations, which can also be seen in Figure 8, with the by-product of turning the particle into a remora. As Figure 9 shows, though the pressure is still the dominant force, the accumulated momentum in the direction of travel is controlled by the contributions from the viscosity term.

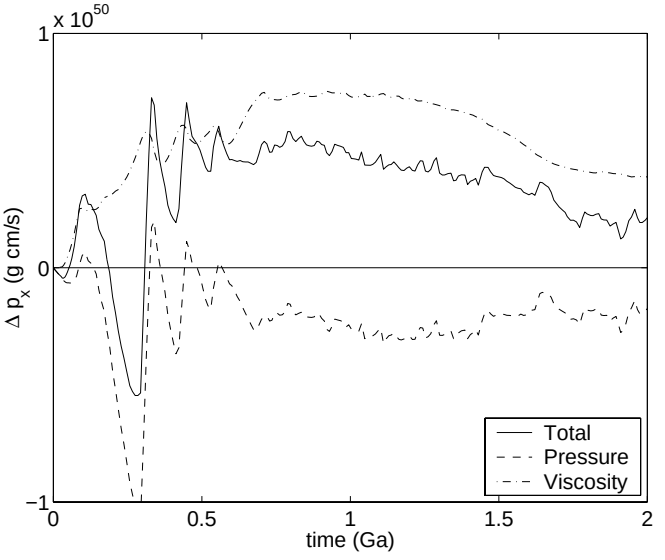

FIG. 9.—Cumulative momentum gained by a remora particle due to SPH forces as a function of time. Plotted is the total momentum boost (*solid line*) as well as the contributions from the SPH pressure term (*dashed line*) and the artificial viscosity (*dash-dotted line*).

5.2.2. *The Significance of a Compact Core*

The previous description of the problem indicates that the compact nature of the clump exacerbates the problem of the creation of a shell of remoras. The hypothesis may be tested directly by having the clump particles occupy a larger volume within their smoothing radius and then determining the drag. The tests correspond to set 6 in § 4.

For this test, the cold clump particles were forced to form a more extended clump by modifying the form of the gravitational potential to produce a repulsive force at close distances. The influence of the antigravity force extends to beyond twice the gravitational softening length to compensate for the strong compressional forces exerted by the pressure of the surrounding hot gas. As such, this form does not permit a stable clump to exist in isolation *and is not proposed as a solution to the problem.* We will hold the velocity of the cold clump fixed as it progresses through the hot medium to allow a stable configuration to develop before the drag on the clump is measured.

The drag for this more diffuse clump was 4.2×10^{35} dyne, which is $\frac{1}{3}$ less than that for the compact clump, found earlier to be 6.0×10^{35} dyne. The factor is remarkable, considering that the diffuse clump has a larger cross section. The cross sections may be measured by convolving the clump particle positions with their effective smoothing radius for interaction with the hot particles, h_{ij}, to produce a column density distribution. The extended clump is found to have a cross section that is 60% larger than that of the compact core. Taken together, these factors imply that the effect of the abrupt transition between the cold clump and the hot particles caused by having a very small central clump *doubles* the drag. The result is a clear demonstration of the significance of a compact core in enhancing the drag.

Thacker et al. note in a similar set of tests a difference in the clump sizes depending on the viscosity form adapted. It reports that a Monaghan-type artificial viscosity, as used in these tests, produces a clump that is 2–3 times more extended than those that use a $\nabla \cdot \boldsymbol{v}$ form. It should be emphasized that the mean interparticle spacing of the cold clump particles was required to be expanded by a factor of 100 before the drag was diminished. Hence, the increase in drag is not something that can be easily fixed by modifying the implementation of SPH. Solving the problem is particularly challenging since expanding the clump leaves it more susceptible to disruption through pressure and tidal stripping, a feature that would worsen the overmerging problem.

6. DISCUSSION

Using a series of simulations of a cold clump moving through a hot medium, we have explored the nature of drag modeled by smoothed particle hydrodynamics in scenarios directly relevant to cosmological structure formation. The results are scale-invariant and, consequently, may be applied to a variety of astrophysical situations. Indeed, any hydrodynamic simulation using the SPH technique in which drag on resolution-limited objects is significant will be affected by the results described herewith.

An analytical expression for the expected amount of drag on the clump permitted the determination of effective radii for the clumps in the various tests.

Our results show the following:

1. There is an excessive amount of drag on resolution-limited clumps at sub-Mach velocities.

2. This effect was found to be owing to the method SPH uses to calculate pressure forces, which is sensitive to large gradients in density.

3. The effective radius of the clump scales with the combined average of the smoothing lengths of both the clump gas and the hot gas.

4. As a consequence of (3), the increase in drag as the clump moves into a denser medium is offset partially by the decrease in the smoothing length of the particles in the medium.

The effective radius at sonic and supersonic velocities was found to agree well with the estimate of twice the average of the smoothing lengths for the hot gas and the cold clump. The scaling with the average smoothing length is independent of the local velocity of sound. Hence the results, if parametrized by the Mach number, are invariant with changes in local sound speed and, consequently, thermodynamic properties of the gas. There are two immediate implications of this scaling: the method of force symmetrization (which determines the method of averaging) affects the drag, and the effective cross section of the clump varies with the density of the medium through which it is traveling.

In regard to the first implication, the method of force symmetrization is selected during the coding of the SPH implementation. There are at least four methods: arithmetically averaging the kernels, or averaging the smoothing radii of the interacting pair of particles using either arithmetic, harmonic, or geometric averaging. It was verified that harmonic averaging of the smoothing radii produces the smallest effective cross section whereas kernel averaging produces the largest. The effect is substantial, with the drag produced by the kernel being on average 2.4 times larger than that of the harmonic averaging. The drag forces from geometric and arithmetic averaging of the smoothing lengths fall in between, with the arithmetic averaging being the larger of the two.

Concerning the second implication of the cross-sectional radius scaling with h_{ij}, it was shown that there is a loss of proper scaling of the drag with density. The drag should scale with density as $F \propto \rho$. The relation is broken because the average smoothing length, h_{ij}, also varies with the density of the surrounding medium. Higher densities lead to a smaller average smoothing length, which decreases the cross-sectional area of the clump, offsetting the increase in drag due to the increased density. This numerical phenomenon is particularly true for methods of force symmetrization that use kernel averaging or arithmetic averaging of the smoothing lengths. For these, the drag on a clump is proportional to $\rho_{\rm hot}^{1/3}$ instead of $\rho_{\rm hot}$. For geometric averaging, this relation changes to $\rho_{\rm hot}^{2/3}$, while for harmonic averaging, the effect is present over a limited range of $h_{\rm hot}/h_{\rm clump}$.

The attenuation of the drag as the density increases will have consequences in simulations of the hierarchical formation of cosmological structure. A disproportionate amount of deceleration will occur in the outer halos of the structures. The biased deceleration will preferentially deposit energy in the outer halo as well as alter the spatial distribution of the deposited matter.

The energy lost from the simulated clumps as they decelerate is deposited locally in the case of the subsonic clump. For a sonic and supersonic clump, SPH successfully models a bow shock, which carries away the energy from the clump, depositing it over a larger volume. The preferential deposition of energy in the outer part of halos should directly

affect the velocity and spatial bias of the baryonic material in the structures.

More significant is the dramatically large drag felt by subsonic clumps. The transition is gradual, with the effective radius scaling as $R_{\rm eff} \propto \mathscr{M}^{-1/2}$ for $\mathscr{M} < 2$. The numerical phenomenon was demonstrated to be a by-product of the method of force calculation used by SPH. For clumps traveling at $\mathscr{M} \lesssim \frac{3}{4}$, the method SPH uses to calculate the hydrodynamic forces, coupled with the compact nature of the cold clump, initiates a process that accretes hot particles on to a sphere about the cold clump. The remora particles are forced by the interaction with the cold clump to oscillate outside the radius of twice the averaged smoothing radius. The oscillation triggers the artificial viscosity, which boosts the velocity of the hot particles to match that of the cold clump. The process is inherent to the SPH method since it arises from the nature of the force calculation which derives the local pressure from the SPH estimate of the local density. Boosting the volume in which the cold clumps reside by providing a short-range antigravity force is shown to reduce the drag by a factor of 2. The modification is not a viable solution to the problem, however, since the clumps are then not stable outside a hot halo.

The accretion of the remoras leads to an increase in drag by increasing the effective cross section. The flow of the particles in Figure 5 indicates that the gas particles are not being repulsed solely by the clump, but also by the remoras in the shell about the clump. If this is the case, then the cross sectional radius should increase from $2h_{ij}$ to $2(h_{ij} + h_{\rm hot})$. For the systems presented here, this should increase the cross-sectional radius by 2.5 times.

Comparing the effective radii calculated for the Mach $\frac{1}{3}$ clump with those of the Mach 1, and Mach 2 clumps implies respective ratios of 1.4 ± 0.1 and 1.9 ± 0.1 (see Table 1 for the radii). However, Figure 2 shows that the change in $R_{\rm eff}$ does not occur as a step function, it is gradual. The previous argument suggests that the ratio may plateau at a value of 2.5 as the velocity drops, but this behavior was not verified. The possibility of a plateau implies a limited range for the relation given by equation (4). At even lower velocities, other phenomena may occur, such as "crystallization" of the clump into the matrix of the hot gas particles as the velocity of the clump approaches the velocity dispersion of the hot gas particles (not the thermodynamic velocity dispersion, but the dispersion due to the "vibration" of the particles [Lombardi, Sills, & Shapiro 1998]).

For virialized objects, the thermodynamic velocity dispersion of the component structures should be on the order of the speed of sound of the halo gas. This velocity is approaching that at which the accretion of remoras commences and we observe the increase in the drag. The increase will enhance the merging rate of the structures (by an amount that is admittedly dependent on other aspects of the simulation such as the stability of the dark-matter halos). Not only will this modify the distribution of small-scale structures, but it will affect the velocity and spatial bias of the baryons.

What may be required to alleviate the problem is a decoupling of the separate hot and cold phases, similar to that described in Pearce et al. (1999). Pearce et al. describe a modification to SPH in which density calculations for particles do not include contributions from particles that are hotter or cooler by some fixed amount. The modification alleviates the supercooling phenomena noted in SPH simulations of clusters (see, e.g., Thacker et al.). As a consequence of the decoupling of the density estimation, the hot particles would not "see" the cold clump when calculating their local density and would not be subjected to the corresponding erratic change shown here. However, the local pressure gradient, which is not decoupled, would still oscillate between being at the edge of a void and at the edge of a dense object as a particle travels from $2h_{ij}$ to within h_{ij} of the cold clump. The phenomenon is ubiquitous to any SPH implementation that does not fully decouple the hot and cold phases, even one that fixes the number of neighbor particles, finding the appropriate value of h_i in each iteration. The oscillation would still occur, but at a potentially reduced rate.

The multiphase SPH method of Ritchie & Thomas (2001) takes a different, and ultimately, more ideal approach. In this method, density is not estimated by an SPH method at all. Instead, the pressure is estimated by the SPH method, and the density is derived from the equation of state. Since pressure gradients are more likely to be smooth when the dynamic time is shorter than the thermal time (the common state within cosmological simulations) the gradients are not as steep and, consequently, not as likely to skew the SPH calculation. Using a series of tests similar to those described here, Ritchie & Thomas demonstrate a reduction in the drag on subsonic clumps of matter to levels in accordance with those predicted in § 3.

Though either of these modifications will lessen the excessive drag at low velocities, neither will remove the scaling of the effective radius with the local number density.

We acknowledge NATO CRG 970081, which facilitated our interaction. We would like to thank R. Thacker for supplying the various implementations of SPH. This work was supported by NSERC Canada.

APPENDIX

DRAG EQUATIONS

In what follows, we will review the relevant equations required to determine the drag felt by a sphere moving through a neutral gas.

The drag on a sphere moving through a fluid medium at any speed is given by the equation (1). The only important parameters relating to the sphere are radius, R, and velocity, V, relative to the medium. The significant parameters of the gas are its density, ρ_g, and temperature, T. The drag is a function of R, V, and ρ_g, as well as the coefficient of drag for a sphere, C_D. The coefficient of drag, in turn, is a function of the Reynolds number, Re, which is a function of the size and velocity of the sphere, as well as the dynamic velocity, η. The dynamic viscosity is peculiar only to the parameters of the enveloping medium and is the biggest unknown.

The coefficient of drag for a sphere or disc, C_D, is defined by equation (1) and usually measured experimentally as a function of the Reynolds number, Re. The Reynolds number, a dimensionless parameter that is essentially the ratio of the size of a disturbance to the size of disturbances that are easily damped, is given by

$$\mathrm{Re} = \frac{RV\rho}{\eta} . \tag{A1}$$

It is not known whether determination of C_D from the results of experiments on centimeter scales is still valid on the scales of galaxies. Nevertheless, the following relation between C_D and Re is found to hold for many scales (Churchill 1988),

$$C_D = \begin{cases} \dfrac{24}{\mathrm{Re}} + \dfrac{3.63}{\mathrm{Re}^{1/2}} - \dfrac{4.83 \times 10^{-3}\mathrm{Re}^{1/2}}{1 + 3 \times 10^{-6}\mathrm{Re}^{3/2}} + 0.49 & \mathrm{Re} < 10^4 , \\ 0.5 , & 10^4 \le \mathrm{Re} < 2 \times 10^5 , \\ 0.2 , & \mathrm{Re} \le 2 \times 10^5 . \end{cases} \tag{A2}$$

The term, 24/Re, is the sole term in Stokes' formula for drag on a sphere, which is a low-Reynolds-number approximation.

The Reynolds number is generally small (~ 1) for the systems we are considering. In the low-Reynolds-number regime, $C_D \simeq 24/\mathrm{Re}$. Combined with equations (1) and (A1), this implies $F_{\mathrm{drag}} \propto V$.

The dynamic viscosity, η, along with the gas density, ρ_g, are the sole parameters relevant to the fluid for calculating the drag. Following Sarazin (1986),

$$\eta \simeq \tfrac{1}{3}\rho_g \langle v \rangle_{\mathrm{rms}} \lambda , \tag{A3}$$

where $\langle v \rangle_{\mathrm{rms}}$ is the mean thermal velocity of the constituent gas particles (molecules, atoms, or ions) and λ is their mean free path.

The mean free path length of the gas particles is on the order of the size of the structure modeled in this paper. That is to say, the Knudsen number is approximately unity where the Knudsen number (Kn) is defined as the ratio of the mean free path length to the diameter of the spherical object passing through it (Chen 1996). For galaxy-sized objects ($Kn \gg 1$) the drag is in the regime of free-molecule flow while for merging clusters it is in the continuum regime.

The mean free path is simply (Lang 1980),

$$\lambda = \frac{\bar{A} m_u}{\rho_g \pi a_o^2} , \tag{A4}$$

where a_o is the diameter of the gas particles. The mean free path is obviously dependent on the assumed composition of the neutral gas, ranging from 5×10^{-11} cm (the Bohr radius) for hydrogen to 10^{-8} cm for neutral atoms and molecules (Cox 2000). The significance of the range is made clearer by noting that, for small Reynolds numbers, $C_D \propto a_o^{-2}$. An intermediate value of $a_o = 10^{-9}$ cm was used. Note that $\eta \propto T^{1/2}$.

REFERENCES

Balsara, D. S. 1995, J. Comput. Phys., 121, 357
Balsara, D., Livio, M., & O'Dea, C. P. 1994, ApJ, 437, 83
Bryan, G. L., Cen, R., Norman, M. L., Ostriker, J. P., & Stone, J. M. 1994, ApJ, 428, 405
Carlberg, R. G. 1994, ApJ, 433, 468
Cen, R. 1992, ApJS, 78, 341
Cen, R., Miralda-Escude, J., Ostriker, J. P., & Rauch, M. 1994, ApJ, 437, L9
Chen, X. 1996, J. Phys. D, 29, 995
———. 1997, J. Phys. D, 2561
Churchill, S. W. 1988, Viscous Flows (Boston: Butterworths)
Couchman, H. M. P. 1991, ApJ, 368, L23
Cox, A. N., ed. 2000, Allen's Astrophysical Quantities Fourth Edition (Berlin: Springer)
Davis, M., Efstathiou, G., Frenk, C. S., & White, S. D. M. 1992, Nature, 356, 489
Evrard, A. E. 1990, ApJ, 363, 349
Evrard, A. E., Metzler, C. A., & Navarro, J. F. 1996, ApJ, 469, 494
Fardal, M. A., Katz, N., Gardner, J. P., Hernquist, L., Weinberg, D. H., & Dave, R. 2000, preprint (astro-ph/0007205)
Frenk, C. S., Evrard, A. E., White, S. D. M., & Summers, F. J. 1996, ApJ, 472, 460
Ghigna, S., Moore, B., Governato, F., Lake, G., Quinn, T., & Stadel, J. 1998, MNRAS, 300, 146
———. 2000, ApJ, 544, 616
Gingold, R. A., & Monaghan, J. J. 1977, MNRAS, 181, 375
Gnedin, N. Y. 1995, ApJS, 97, 231
Hernquist, L., & Katz, N. 1989, ApJS, 70, 419
Horner, D. J., Mushotzky, R. F., & Scharf, C. A. 1999, ApJ, 520, 78
Katz, N. 1992, ApJ, 391, 502
Katz, N., & Gunn, J. E. 1991, ApJ, 377, 365
Katz, N., Hernquist, L., & Weinberg, D. H. 1992, ApJ, 399, L109
Katz, N., Weinberg, D. H., & Hernquist, L. 1996, ApJS, 105, 19
Kay, S. T., Pearce, F. R., Jenkins, A., Frenk, C. S., White, S. D. M., Thomas, P. A., & Couchman, H. M. P. 2000, MNRAS, 316, 374
Klypin, A., Gottlüober, S., & Kratsov, A. V. 1999, ApJ, 516, 530
Lang, K. R. 1980, Astrophysical Formulae (Berlin: Springer)
Lombardi, J. C., Sills, A., & Shapiro, S. L. 1998, preprint (astro-ph/9807290)
Lucy, L. 1977, AJ, 82, 1013
Moore, B., Katz, N., & Lake, G. 1996, ApJ, 457, 455
Moore, B., Katz, N., Lake, G., Dressler, A., & Oemler, A. 1996, Nature, 379, 613
Moore, B., Lake, G., Quinn, T., & Stadel, J. 1999, MNRAS, 304, 465
Mori, M., & Burkert, A. 2000, ApJ, 538, 559
Navarro, J. F., & White, S. D. M. 1993, MNRAS, 265, 271
Nulsen, P. E. J. 1982, MNRAS, 198, 1007
Ostriker, E. C. 1999, ApJ, 513, 252
Pearce, F. R., et al. 1999, ApJ, 521, L99
Persic, M., Salucci, P., & Stel, F. 1996, MNRAS, 281, 27
Ritchie, B. W., & Thomas, P. A. 2001, MNRAS, 323, 743
Ryu, D., Ostriker, J. P., Kang, H., & Cen, R. 1993, ApJ, 414, 1
Sarazin, C. L. 1986, Rev. Mod. Phys., 58, 1
Steinmetz, M. 1996, MNRAS, 278, 1005
Steinmetz, M., & Müller, E. 1993, A&A, 268, 391
Summers, F. J., Davis, M., & Evrard, A. E. 1995, ApJ, 454, 1
Thacker, R. J., Tittley, E. R., Pearce, F. R., Couchman, H. M. P., & Thomas, P. A. 2000, MNRAS, 319, 619
Tittley, E. R., & Couchman, H. M. P. 1999, preprint (astro-ph/9911365)
van Kampen, E. 1995, MNRAS, 273, 295
White, S. D. M. 1976, MNRAS, 177, 717